

Synthesis and characterization of structural and magnetic properties of graphene/hard ferrite nanocomposites as microwave-absorbing material

Zehra Durmus · Ali Durmus · Huseyin Kavas

Received: 21 August 2014 / Accepted: 16 October 2014 / Published online: 25 October 2014
© Springer Science+Business Media New York 2014

Abstract In this study, barium hexaferrite nanoparticles were synthesized via the citrate sol–gel combustion method in a reaction medium consisting of various forms of graphene nanosheet, such as expanded graphite, expanded graphite oxide, and reduced graphite oxide to prepare novel type graphene/hexaferrite nanocomposites as microwave-absorbing material. The microstructural features and physical properties of nanocomposites were characterized by X-ray diffraction, Raman spectroscopy, Fourier transform infrared spectroscopy, scanning electron microscopy, and thermogravimetric analysis methods. Magnetic properties of the nanocomposites were studied by a vibrating sample magnetometer, and the microwave-absorption and -reflection properties of samples were also determined in the frequency range of 8–12 GHz. It was found that the surfaces of the graphene nanosheets were successfully decorated with the barium hexaferrite nanoparticles, and the resulting layered nanocomposite structure showed the reflection loss value of -58 dB at 11.42 GHz.

Introduction

Microwave-absorbing materials have attracted great technical and scientific interests due to their swiftly increasing importance for the specific implementations such as silent rooms, radar systems, and military applications and ability for reducing electromagnetic interference (EMI) and radar signatures for a long time. Electromagnetic (EM) waves can be shielded by either reflecting or absorbing of EM radiation. Various types of materials such as carbon, conducting polymers, metal and metal particles, and alloys can be used to shield EM waves.

The magnetically hard hexagonal M ferrites, having the general formula of $M\text{Fe}_{12}\text{O}_{19}$ where the M designates Ba, Sr, or Pb, are the most commercially used materials of interest for the EM applications such as permanent magnets, magnetic recording media, and electric motors because they exhibit high coercivity and magnetic permeability due to their unique structural property of high magnetocrystalline anisotropy along the *c*-axis of the hexagonal structure. Especially barium and strontium hexaferrites ($\text{BaFe}_{12}\text{O}_{19}$ and $\text{SrFe}_{12}\text{O}_{19}$) have high saturation magnetizations (M_s) of 72 emu g^{-1} and at least 74 emu g^{-1} , respectively. Barium hexaferrite, also named as magnetoplumbite, is the most widely used material among the family of hard magnets for the EM applications due to its attractive magnetic properties, high magnetic anisotropy field (1.7 T) which results in a high coercivity, remanence, and a ferromagnetic resonance at about 50 GHz, high Curie temperature, excellent chemical stability, good corrosion resistance, and low cost [1].

Nanocrystalline form of $\text{BaFe}_{12}\text{O}_{19}$ can be successfully used for the absorption of microwave radiation in a wide frequency range, between 12 and 18 GHz [2]. The ferromagnetic resonance coincides with large magnetic losses,

Z. Durmus (✉)
Department of Pharmaceutical Biotechnology, Faculty of
Pharmacy, Bezmialem Vakıf University, Fatih, 34093 Istanbul,
Turkey
e-mail: zdurmus@bezmialem.edu.tr

A. Durmus
Department of Chemical Engineering, Faculty of Engineering,
Istanbul University, Avcilar, 34320 Istanbul, Turkey

H. Kavas
Department of Engineering Physics, Istanbul Medeniyet
University, Kadıköy, 34700 Istanbul, Turkey

making these materials suitable for use in the microwave band as high-frequency absorbers. The resonance phenomena in ferrites can be explained by two different mechanisms: spin resonance and domain-wall motion. Permeability spectrum of polycrystalline ferrites is generally explained by the combination of contributions by both. However, the complex permeability in the high-frequency region is affected by the spin rotation component [3]. The EMI shielding effectiveness of $\text{BaFe}_{12}\text{O}_{19}$ has also been extensively studied [4–8]. The EM properties of microwave ferrites depend on the structural and physical features of these materials such as chemical composition, crystal structure, crystallite size, particle size, etc. It is also well known that the size of magnetic particles is influenced by the synthesis method employed (e.g., co-precipitation, sol-gel, hydrothermal growth, citrate combustion, surfactant-assisted decomposition, etc.) and thermomechanical parameters during the preparation process (e.g., mixing method, reaction time, temperatures of annealing, sintering, and calcination). Pardavi-Horvath reviewed the effects of types and chemical composition of ferrites on the physical properties and related microwave applications of such materials [9]. It has been pointed out that the most significant magnetic properties of ferrite materials, namely M_s , coercivity, magnetization, and loss, change dramatically when the particle size is reduced to nanoscale [3]. It is generally considered that this property change is due to the fact that the size reduction in the magnetic materials yields higher surface/volume ratio which leads to different properties than the bulk materials. Decreasing in the particle size results in reduction in the number of spins cooperatively linked within the particle and surface effects becomes much more important on the magnetic properties of particles. Changes in the magnetic properties of particles depending on the size of particles can be easily monitored by hysteresis loops that provide information about the manipulation of microwave-absorption frequency. Peddis et al. investigated the effect of structural variations on the magnetic properties of cobalt ferrite (CoFe_2O_4) nanoparticles and also discussed the effects of particle size on the physical properties of these materials [10]. They also reviewed the structure–property relationships of the magnetic nanoparticles in detail and concluded that the magnetic properties of nanoparticles were mostly influenced by particles size, while the magnetic anisotropy and interparticle interactions played a fundamental role in the physics of these systems. Crystallite size of magnetic nanoparticles is another important parameter on their magnetic properties [11–13]. Deraz studied on the size- and crystallinity-dependent magnetic properties of copper ferrite (CuFe_2O_4) nanoparticles prepared by a combustion route and reported that the magnetization values of samples increased with the increasing of particle size [11]. It was also shown by Deraz

that the M_s value of Cu-ferrite possessed a linear relationship with both the crystallinity and the crystallite size. Chia et al. investigated the size- and crystallinity-dependent magnetic properties of cobalt ferrite (CoFe_2O_4) nanocrystals synthesized by a wet chemical co-precipitation method [12]. They found that the degree of crystallinity and mean crystallite size of CoFe_2O_4 nanocrystals increased with the increasing synthesis and subsequent calcinations temperature which improved the magnetic properties of samples.

Carbon-based materials, e.g., single or multiwall carbon nanotubes, graphene, carbon fiber, and carbon black can also be used as alternative conducting materials for the EMI shielding applications. Magnetic functionalization of carbon materials has been considered as an innovative alternative to create multifunctional carbon/magnetic hybrid materials for specific applications especially in shielding of EM waves in a wide range of frequency. Preparation and characterization of such materials is also a rapidly expanding research area since the composite structure allows obtaining suitable candidates for EM wave absorber with a low reflectivity at microwave frequencies. These studies have focused on the preparation and characterization of carbon nanotube (CNT) decorated with various types of magnetic nanoparticles [14–18]. Zhao et al. prepared a nanocomposite, uniformly coated CNT with strontium ferrite nanoparticles, by the in situ sol-gel reaction [19]. They reported that the coercive force of the samples increased with the increasing CNT content into the structure. Correa-Duarte et al. magnetically functionalized CNT with iron oxide (Fe_3O_4) nanoparticles via polymer wrapping and layer-by-layer assembly techniques [20]. Georgakilas et al. employed a carboxylic derivative of pyrene as an interlinker for the attachment of capped magnetic nanoparticles on the CNT surfaces [21]. They also reported that this route enhanced the solubility of CNTs in organic solvents. He et al. investigated the microwave-absorbing properties of single-wall carbon nanotube (SWCNT)/ $\text{BaFe}_{12}\text{O}_{19}$ nanocrystalline composites in the frequency region of 2–18 GHz [22]. They found that the maximum reflection loss (RL) of the SWCNT/ $\text{BaFe}_{12}\text{O}_{19}$ composite with a thickness of 3 mm reached 30.79 dB at 10.5 GHz and concluded that the microwave-absorption properties of composite are evidently improved due to the multiple absorptive mechanisms. Ghasemi et al. prepared magnetic multiwalled carbon nanotube (MWCNT) composites by the assembly of Mg–Ni–Ti-substituted barium ferrite nanoparticles onto surface of MWCNT and examined the magnetic properties of the samples by the vibrating sample magnetometer (VSM) technique at room temperature [23]. They reported that the composites display a great potential application as wide-band EM wave absorbers based on the RL data. Li et al.

prepared polyaniline/strontium ferrite/MWCNT composites by synthesizing strontium ferrite particles by sol–gel method and self-propagating synthesis followed by in situ polymerization [24]. They declared that the EM properties of composites were excellent in the frequency range of 2–18 GHz, which mainly depend on the dielectric loss in the range of 2–9 GHz, and mainly on the magnetic loss in the range of 9–18 GHz.

Another unique structure of carbon is graphene, the “thinnest material in our universe” [25] and a flat monolayer of hexagonally arrayed sp^2 -bonded carbon atoms tightly packed into a two-dimensional (2D) crystal of hybridized carbon with honeycomb lattice. Graphene is the basal building block in all graphitic materials [26]. Graphene nanolayers can be prepared from the graphite particles by chemical and/or physical treatments [27–30]. The unique structural features and geometric advantages of layered carbons make the graphene an ideal, alternative, and high-performance supporting material to prepare novel functional nanomaterials. Especially, graphene sheets decorated with magnetic nanoparticles could exhibit good magnetic, electrical, and dielectric performance and great application potential in the fields of EM and radio-frequency interference (RFI) materials, electrochromic devices, Li ion batteries, sensors, actuators, and field-effect transistors [31].

Syntheses of soft ferrites onto various types of nano-sized graphitic templates such as graphene [32–35], graphite [36–38], and graphene oxide [39–42] have been studied. Bai et al. prepared magnetic reduced graphene oxide–ferrite hybrids according to one-pot solvothermal synthesis method and used the resulting hybrids for the removal of organic dyes, rhodamine B (RhB), and methylene blue (MB) [43]. They showed that monodispersed MFe_2O_4 microspheres with uniform size were homogeneously deposited on reduced graphene oxide nanosheets. They also reported that the hybrids possessed considerable saturation magnetization, lower remanence, and coercivity, and importantly they can be used as effective adsorbents for dye removal.

To the best of our knowledge, only a few studies have been published on the preparation and characterization of carbon/hard ferrite nanocomposites. Yang and Wang prepared $BaFe_{12}O_{19}$ /NanoG composite by the precipitation of barium hexaferrite on the surface of graphite nanosheets [44]. They reported that the RL values of the composite structure were found to be in the range of about 16–17 dB in the frequency range of 8–12 GHz. Bhattacharya et al. synthesized magnetic M-type hexaferrite, $CuFe_{10}Al_2O_{19}$ (CFA)/graphene and CFA/graphene/polyaniline (PANI) composites by facile chemical co-precipitation and in situ methods by means of acid modified graphene [45]. They reported that the prepared multifunctional composites

exhibited an outstanding and improved microwave-absorption performance, and the electrochemical properties compared to the pristine graphene and CFA. It was also declared that the introduction of PANI into the structure improved the microwave absorption and specific capacitance of the composites.

In this study, barium hexaferrite nanoparticles were synthesized onto various types of graphene sheets such as expanded graphite (EG), expanded graphite oxide (EGO), and reduced expanded graphite oxide (rEGO) by the citrate sol–gel combustion method. In this method, nano-thick graphene sheets were efficiently decorated with barium hexaferrite nanoparticles to prepare novel nanocomposites which possibly exhibit the microwave-absorbing performance. Structural properties and microwave absorption performances of the samples were characterized, in detail.

Experimental section

Materials

Iron (III) nitrate nonahydrate, $Fe(NO_3)_3 \cdot 9H_2O$, barium nitrate ($Ba(NO_3)_2$), citric acid ($C_6H_8O_7$), sulfuric acid (H_2SO_4 fuming), hydrogen peroxide (30 % H_2O_2), potassium permanganate ($KMnO_4$), ammonia solution (28 % NH_3), sodium nitrate ($NaNO_3$), hydrazine hydrate ($N_2H_4 \cdot H_2O$), and hydrochloric acid (37 % HCl) were all purchased from Merck and Sigma-Aldrich. All the chemicals employed in the study were of analytic grade and used as-received without a purification. The EG was a commercial grade, thermally expanded product (TIMREX[®] BNB90), kindly provided by TIMCAL (Switzerland). The density, surface area, average particle size (d_{90}), and the oil adsorption number (OAN) values of EG were reported as 2.24 g cm^{-3} , $28 \text{ m}^2 \text{ g}^{-1}$, $85.2 \text{ }\mu\text{m}$, and $150 \text{ ml } 100 \text{ mg}^{-1}$, respectively, by the producer.

Graphite modification

Chemical oxidation and reduction are the well-known modification methods of layered carbon particles to obtain graphene nanosheets. In the first step, EG was oxidized by the modified Hummers [46] method to prepare EGO. In this method, the EG powder was dispersed in H_2SO_4 , and then the $NaNO_3$ and $KMnO_4$ were gradually introduced in this suspension and vigorously stirred at the temperature below $20 \text{ }^\circ\text{C}$ into an ice bath for 3 h. Then, the reaction mixture was diluted with deionized water in an ice bath to keep the temperature below $100 \text{ }^\circ\text{C}$. The H_2O_2 (30 wt%) was slowly added into the suspension, and the mixture was stirred for 2 h. It was observed that the brownish color of mixture turned into a brilliant yellow which indicates strong oxidation. The mixture was centrifuged and washed

several times with an aqueous solution of 5 % HCl. Then, it was washed repeatedly with deionized water until the pH of the supernatant became neutral. A brown powder of EGO was obtained and dried in a vacuum oven at 60 °C.

In the second step, EGO powder was dispersed in the deionized water in a flask, and a stable yellow–brown dispersion was obtained due to the hydrophilic nature of EGO. Hydrazine monohydrate, which is the most frequently used reducing agent due to the simplicity of its application procedure and the reduction efficiency to obtain graphene sheet having excellent physical properties [47], was then added to the EGO suspension. The flask equipped with a water-cooled condenser was heated up to 100 °C in an oil bath and kept at this temperature for 24 h. The EGO sheets were reduced to form graphene nanosheets or rEGO, and gradually precipitated out as a black solid due to the hydrophobic nature of rEGO sheets. It is well known that the physical and chemical properties of nanosheets such as the thickness, surface character, and surface area strongly depend on the experimental parameters of oxidation and reduction procedures. The rEGO was isolated by filtration and washed with the excess of water and methanol and then dried in an air-circulating oven.

Synthesis of graphene/BaFe₁₂O₁₉ nanocomposites

The synthesis process of graphene/BaFe₁₂O₁₉ nanocomposites is schematically illustrated in Fig. 1. The rEGO powder was first dispersed in deionized water by sonication for 1 h to transform the carboxylic acid groups to carboxylate anions. In this study, the citrate sol–gel combustion method was applied to synthesize BaFe₁₂O₁₉ nanoparticles. Stoichiometric amounts of Fe(NO₃)₃·9H₂O and Ba(NO₃)₂ (Fe/Ba ratio of 11) were dissolved in a minimum amount of deionized water by stirring at 50 °C. Citric acid was then added to the solution of Ba²⁺ and Fe³⁺ to chelate these ions by adjusting the molar ratio of citric acid/metal ions as 1:1. This solution was added dropwise to the rEGO suspension at room temperature, and the mixture was vigorously stirred under a nitrogen flow for 30 min. Then, ammonia was added to the mixture to adjust the pH value to 7. The suspension was slowly evaporated to form a viscous black gel by keeping the temperature of mixture at 80 °C and stirring constantly. The precursor gel was transferred to an evaporating dish and heated up to temperature in the range of 140–150 °C. At this step, the precursors gel was self-ignited and combusted rapidly to form a brown powder as seen in Fig. 1. The resulting self-standing fluffy powder of rEGO/BaFe₁₂O₁₉ nanocomposite was pre-calcined at 450 °C for 4 h and then sintered at 1100 °C for an hour. The synthesis route was also repeated by means of EG and EGO powders to prepare EG/BaFe₁₂O₁₉ and EGO/BaFe₁₂O₁₉ nanocomposites to compare the structural and microwave-absorbing performances of such material to the rEGO/BaFe₁₂O₁₉.

Structural and physical characterizations of samples

The microstructural and morphological properties of EG, EGO, rEGO, and nanocomposite samples were characterized by X-ray diffraction (XRD), Fourier transform infrared spectroscopy (FTIR), Raman spectroscopy, and scanning electron microscopy (SEM) methods. The XRD patterns of samples were obtained using a Rigaku Smart Lab. XRD with Cu-K_α radiation at room temperature. FTIR spectra were recorded in transmission mode using a Perkin Elmer BX-FTIR infrared spectrometer using the KBr pellets of sizes in the range of 400–4000 cm⁻¹ and with the resolution of 2 cm⁻¹. The Raman spectra of graphitic materials were also recorded in a Thermo-Fisher Scientific, DXR dispersive Raman instrument using laser excitation of 532 and 780 nm and an InGaAs detector, in the range of 400–3500 cm⁻¹. One hundred scans were accumulated with the resolution of 4 cm⁻¹ by means of a laser power of 100 mW. The morphological features of samples were investigated by a field emission SEM (FE-SEM, FEI Quanta FEG 450) operated at 30 kV. Powder samples were directly imaged in the electron microscope after a proper preparation of sample sputter-coated with gold.

Magnetic properties of the samples, all in powder form, were characterized using a VSM (LDJ Electronics Inc., Model 9600) at room temperature, with an applied field of 15 kOe. The thermal properties of EG, EGO, and rEGO were analyzed with a thermogravimetric analyzer (TGA), SII Nanotechnology TG/DTA 6300, at the heating rate of 10 °C min⁻¹ in the temperature range of 30–800 °C, under the nitrogen atmosphere with the gas flow rate of 50 ml min⁻¹.

Powder samples shaped as a rectangular sheet with the dimensions of 10.2 × 22.8 × 2 mm in length, width, and thickness, respectively, by pressing using a metal mold for the microwave-absorbing measurements. Microwave-absorption measurements were performed using a vector network analyzer (VNA), HP 8510C, in the frequency range of 8–12 GHz. The scattering parameters of samples for the reflection (S₁₁ or S₂₂) and absorption (S₁₂ or S₂₁) were determined. Full two-port calibration was performed to remove some errors due to the directivity, source match, load match, etc., in both forward and reverse directions.

Results and discussion

Structural and morphological characterization of samples

Figure 2a shows the XRD patterns of EG, EGO, and the chemically reduced graphite oxide sheets with the diffraction angle in the range of 5–40°. It is clearly seen that the commercial EG exhibits a characteristic sharp and

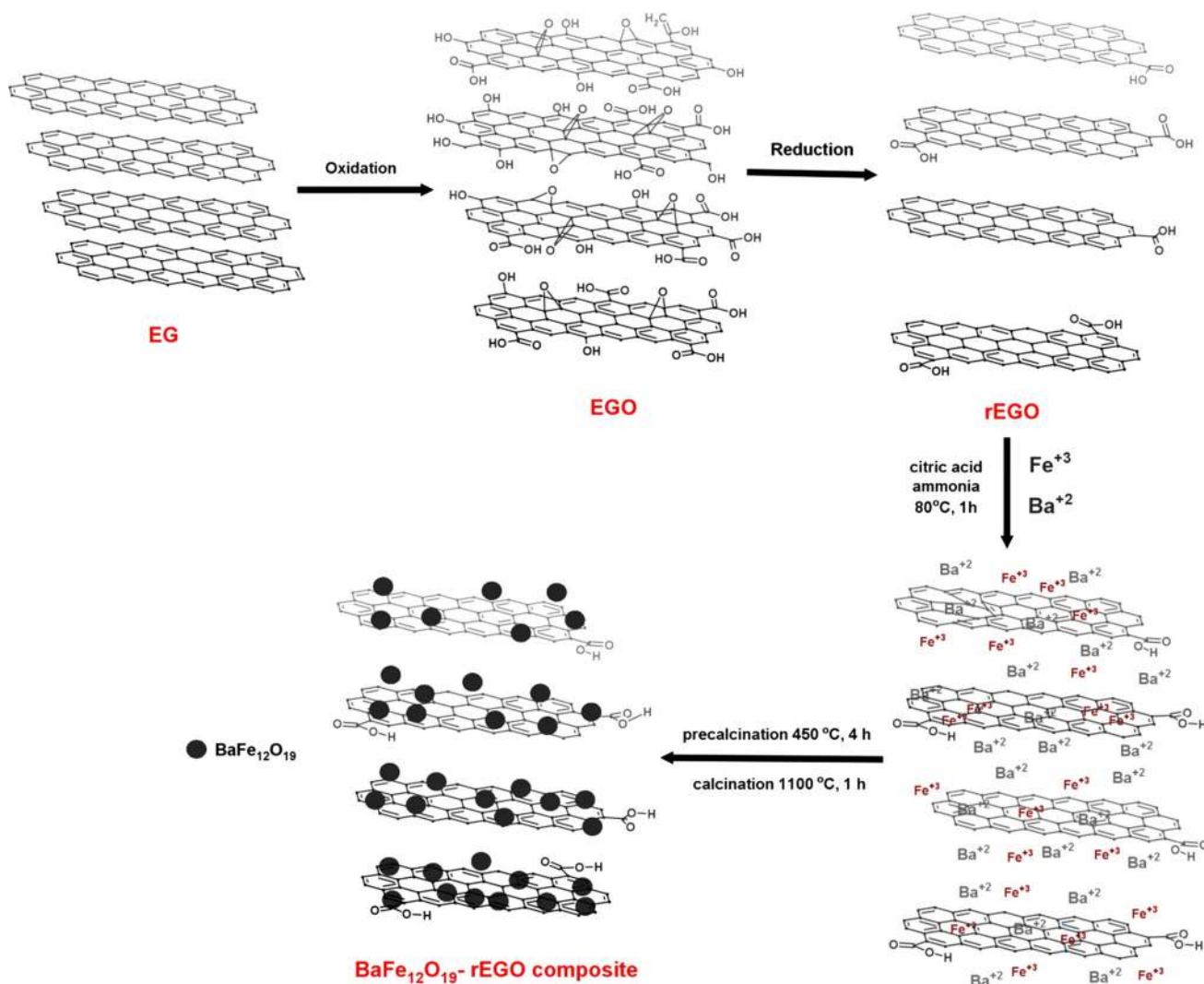


Fig. 1 A simple synthesis route for the preparation of graphene/barium hexaferrite nanocomposites

intense peak at the diffraction angle of 26.5° which corresponds to the d_{001} planes of graphite. Intergallery distance between the graphene sheets was calculated by the Bragg’s equation as defined in the Eq. (1);

$$\lambda = 2d\sin\theta \tag{1}$$

where d is the spacing between sheets; λ , the wavelength of X-ray (0.154 nm); and θ , the angle of diffraction. The intergallery distance between the graphite sheets was calculated to be 0.336 nm for the EG. This value is the characteristic d_{001} space between the graphene layers in the graphite. As clearly seen in the figure, the d_{001} peak shifted to the lower diffraction angle ($2\theta = 11.3^\circ$) which corresponds to intergallery distance of 0.782 nm for the EGO. Another important issue is that the characteristic d_{001} peak of EGO is much broader and less intense than that of EG. This is obviously due to the intercalation of chemical

species through intergallery spaces and expansion of graphene layers by the oxidation in a strong acidic medium according to the modified Hummer’s method. Chemically reduced graphene oxide exhibited two broad peaks at the diffraction angles of 12.2° and 24.8° which can be attributed, respectively, to the d_{001} and d_{002} planes of graphene sheets. It is well known that the chemical reduction of GO removes the organic species onto the graphene layers. A formation of fully exfoliated, “house-of-card” structure consisting of disordered graphene sheets might be expected by chemical treatment. Based on the XRD result given in Fig. 2a, it can be concluded that the expansion of graphene stacks was successfully achieved by the oxidizing agents, but, the chemical reduction did not yield a fully exfoliated structure. The broad and small peaks observed in the XRD pattern of rEGO can be attributed to the facts those the organic groups did not completely removed from the sheets and but the

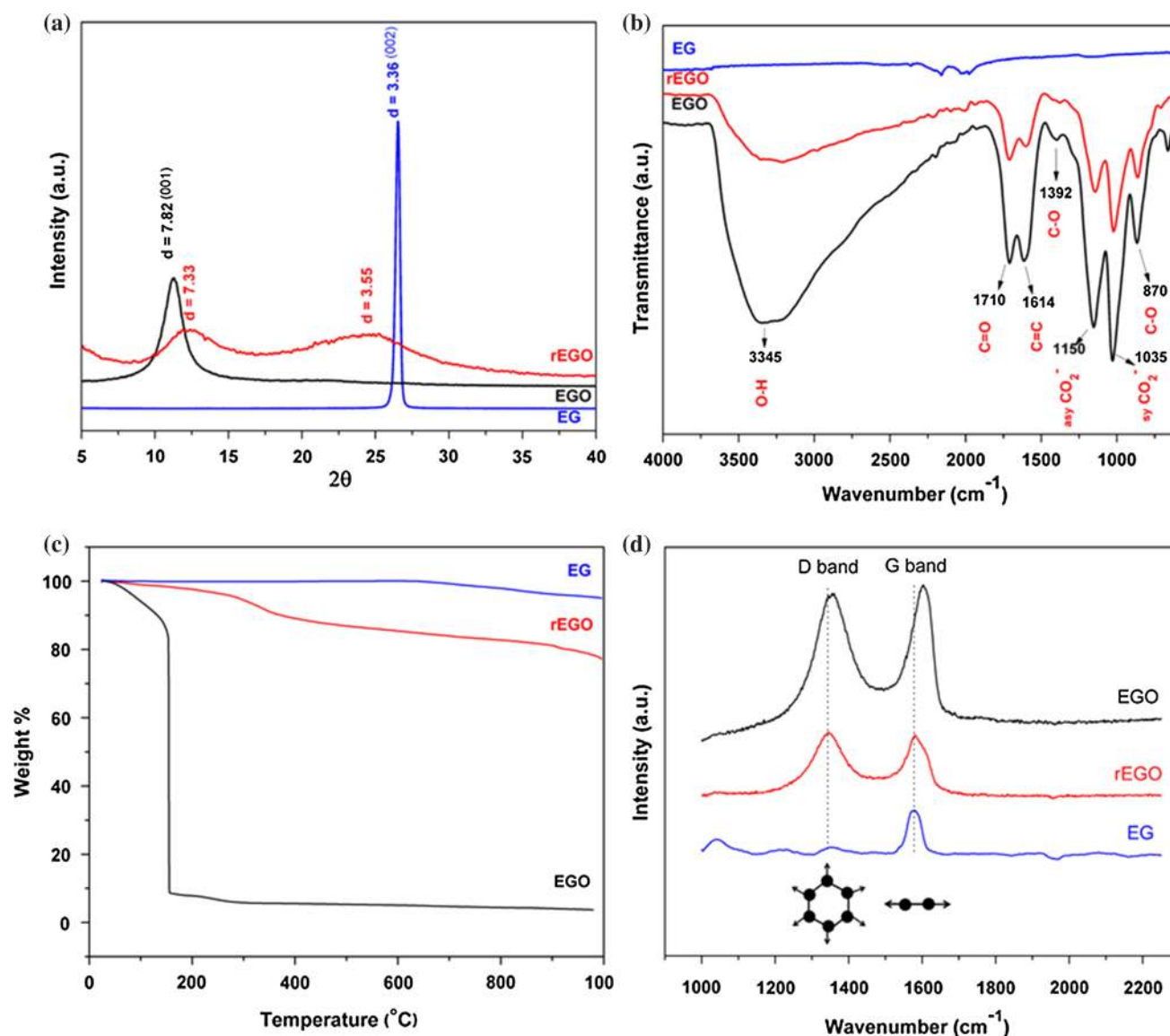


Fig. 2 **a** XRD patterns, **b** FT-IR spectrum, **c** TGA thermograms, and **d** Raman spectrum of EG, EGO, and rEGO

resulting product probably formed highly exfoliated structure consisting of stacks with few layers of graphene sheets.

Figure 2b shows the FTIR spectra of EG, EGO, and rEGO sheets in the wavenumber range of 400–4000 cm^{-1} . As seen, no significant peak was observed in the FTIR spectra of EG. On the other hand, the EGO and rEGO exhibited various peaks due to the presence of different types of oxygen functionalities onto the surfaces. The strong peak observed at 3400 cm^{-1} corresponds to the stretching vibration of O–H. Peaks observed at 1710 and 1614 cm^{-1} belong to the stretching vibration of C=O and the skeletal vibration of unoxidized graphitic domains (aromatic C=C), respectively. Furthermore, the characteristic peaks observed at the wavenumbers of 1392, 1150, 1035, and 870 cm^{-1} correspond to the stretching of C–O,

asymmetric and symmetric stretchings of carbonyl groups $-\text{CO}_2$, and stretching of C–O bonds, respectively. It can be seen in the figure that the stretching vibration of O–H at the wavenumber of 3400 cm^{-1} and the stretching vibrations of C=O at the wavenumber of 1710 cm^{-1} were still observed in the rEGO. However, these peaks were smaller than those observed in the FTIR spectra of EGO. These results pointed out that the chemical reduction of EGO with the hydrazine hydride significantly reduced the oxygen species, but some carboxyl groups were still remaining onto the sheets.

TGA thermograms of EG, EGO, and rEGO are given in Fig. 2c. TGA method analysis is another simple tool for quantifying organic species between the graphene layers and probing the effectiveness of oxidation and reduction

reactions. As seen in the figure, EG was highly stable up to 600 °C, as expected. However, the EGO shows a slight mass decrease from room temperature to 150 °C, which can be primarily attributed to the evaporation of volatiles and adsorbed water molecules, and a sharp, step-wise weight loss from 150 °C to 200 °C. This major weight loss was due to the rapid decomposition of the oxygen-containing functional groups which indicated oxidation of graphene layers sufficiently. The rEGO exhibited enhanced thermal stability and much less weight loss compared to the EGO, suggesting that the labile oxygen groups were highly removed from the EGO sheets by the reduction with hydrazine hydrate. Significant weight loss of rEGO started at about 300 °C, and the total weight loss was found to be about 10–12 wt% within the temperature range of 300–900 °C, which can be assigned to the presence of some remaining organic species onto the rEGO sheets.

The Raman spectra of EG, EGO, and rEGO are depicted in Fig. 2d. Raman spectroscopy is a fast and reliable characterization method to understand the structural transformations from graphite to graphite oxide and then to graphene, by analyzing the in- and out-of-plane bondings of hexagonal carbon framework. The starting material, EG, exhibits a sharp *G* band at 1580 cm^{-1} and a weak *D* band, while the EGO displays two distinct peaks at 1356 and 1602 cm^{-1} . The *G* and *D* bands are attributed to the graphitic crystal lattice vibration and defects and disorders in graphitic crystal lattices in the carbon materials, respectively. The intense *D* band observed in the EGO obviously signified that the graphitic edges were successfully modified with the oxygen-containing groups. It was also found that the rEGO shows less intense but clear *D* and *G* bands at 1345 and 1584 cm^{-1} , respectively, which pointed out the organic species remaining onto the graphene sheets after the chemical reduction. Raman spectra results confirm the previously mentioned structural characterization of graphitic samples obtained by the other techniques: XRD, FTIR, and TGA.

SEM micrographs of EG, EGO, and rEGO are shown in Fig. 3a–c, respectively. In Fig. 3a, highly porous and layered structure of commercial EG having large stacks, possibly consisting of hundreds of graphene nanosheets, can be clearly seen. It should also be noted that the surfaces of the EG sheets are quite flat and smooth. Figure 3b shows the SEM micrograph of the oxidized counterpart, EGO. It is worthy to observe that the lateral size of graphitic nanosheets was not disrupted with the oxidation, but the surface properties of modified product were strongly affected. As seen in the Fig. 3b, the surfaces of EGO nanosheets are rough, and the edges are highly crumpled. On the other hand, the SEM image rEGO shown in Fig. 3c clearly signifies that the very thin, wrinkled, and transparent graphene sheets having the lateral size in the range

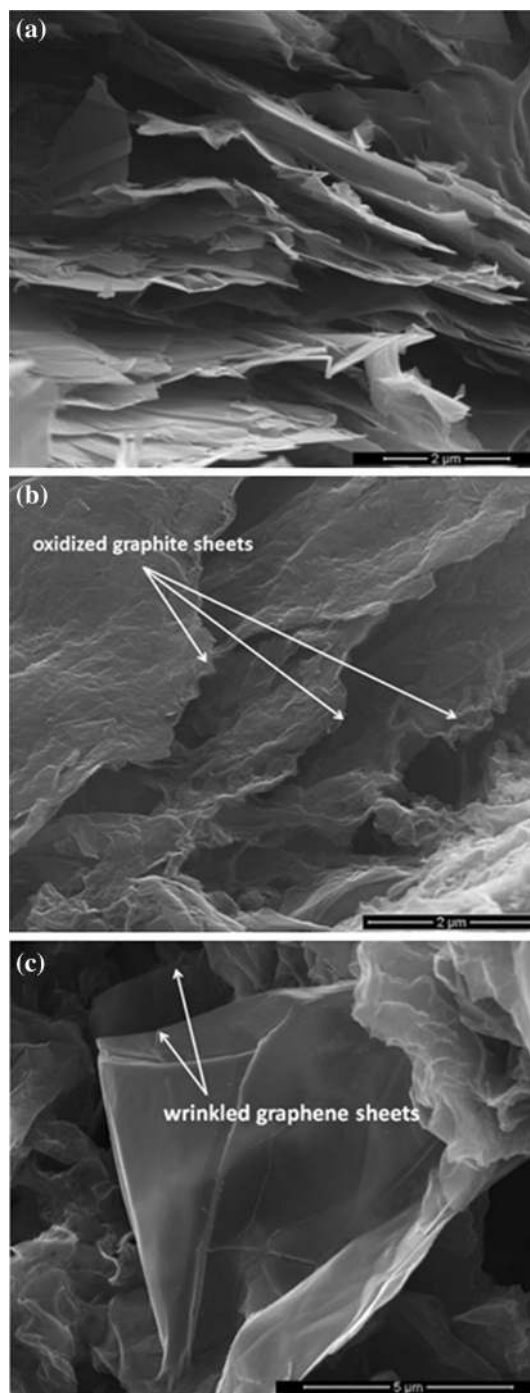


Fig. 3 SEM micrographs of **a** EG, **b** EGO, and **c** rEGO nanosheets

of 5–10 μm were successfully obtained by the chemical reduction.

XRD patterns of nanocomposites are given in Fig. 4. These patterns indicate the formation and the crystal structure of $\text{BaFe}_{12}\text{O}_{19}$ synthesized onto the EG, EGO, and rEGO sheets. The characteristic miller indices of (110), (008), (112), (107), (114), (200), (108), (203), (205), (118),

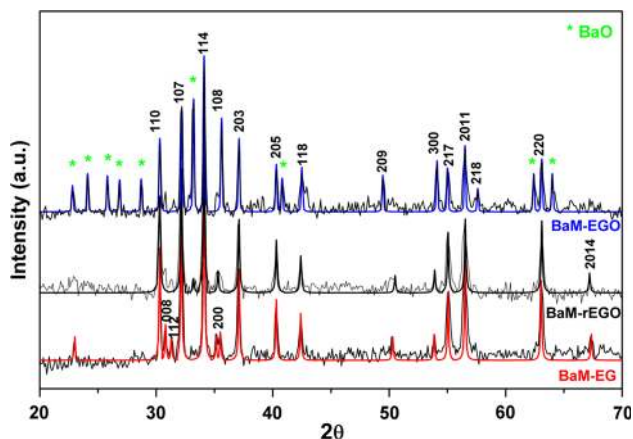


Fig. 4 XRD patterns of BaM-EG, BaM-EGO, and BaM-rEGO nanocomposites

(209), (300), (217), (2011), (218), (220), and (2014) were assigned on the patterns. All the characteristic peaks indexed by the cubic structures of $\text{BaFe}_{12}\text{O}_{19}$ (JCPDS no. 84-0757) revealed that the highly pure hexaferrite phase were formed. As seen in the figure, diffraction peaks, which correspond to the structure of $\text{BaFe}_{12}\text{O}_{19}$, are very sharp and intense, which indicates to small crystallite size. In the XRD pattern of BaM-EGO, some peaks belong to the BaO were also observed. However, it was found that the diffraction peaks of BaO disappeared by using the rEGO as the substrate material.

The average size of crystallites was determined by fitting the diffraction patterns of the samples using the line profile fitting [48]. The average crystallite sizes of $\text{BaFe}_{12}\text{O}_{19}$ were calculated to be 16 ± 4 , 20 ± 3 , and 22 ± 5 nm for the nanocomposites synthesized onto the EG, EGO, and rEGO sheets, respectively. These results represent that the $\text{BaFe}_{12}\text{O}_{19}$ nanoparticles were successfully synthesized onto the various types of graphene sheets. It can also be concluded that the crystallite size of $\text{BaFe}_{12}\text{O}_{19}$ is not dependent on the surface character and the thicknesses of graphene sheets.

FTIR spectra of nanocomposites are shown in Fig. 5, in the wavenumber range of $400\text{--}2000\text{ cm}^{-1}$. Characteristic bands of ferrite structure can be seen in the FTIR spectra of all nanocomposite samples. The absorption bands observed at 415 , 529 , and 572 cm^{-1} correspond to typical M–O bonds in the $\text{BaFe}_{12}\text{O}_{19}$ structure [49, 50]. Absorption bands seen in the spectrum of BaM-EGO at the wavenumber range of $1050\text{--}1200\text{ cm}^{-1}$ can be attributed to the little amount of organic species, mainly carbonyl and carboxyl groups, formed onto the graphene sheets as previously mentioned. However, no peak was observed in this region for the BaM-rEGO sample.

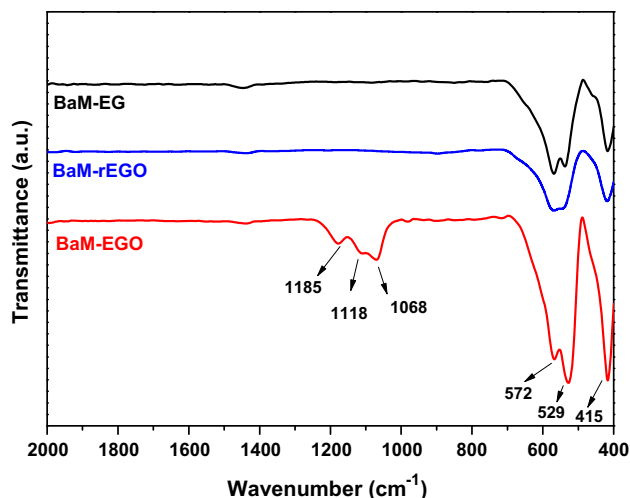
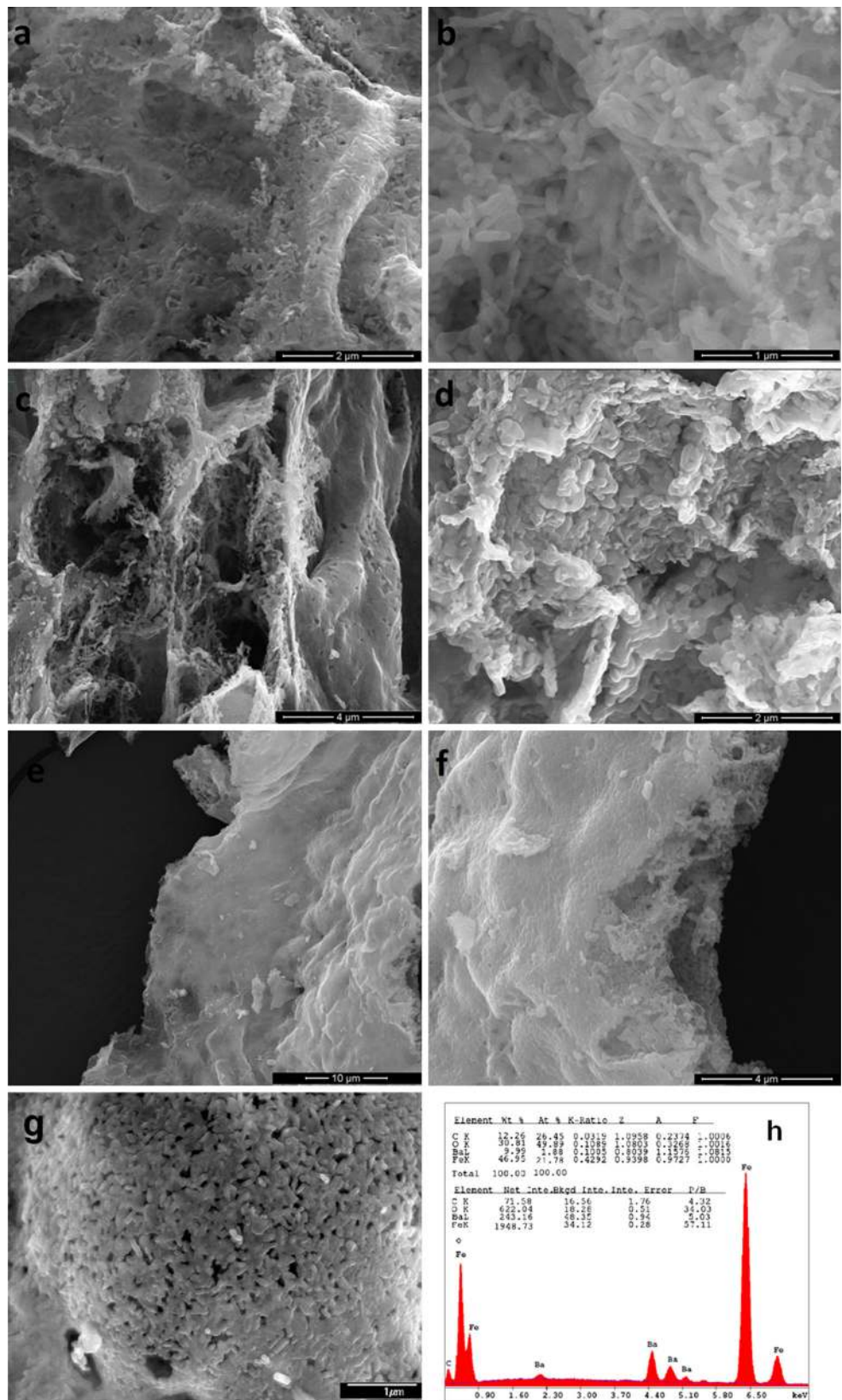


Fig. 5 FT-IR spectrum of BaM-EG, BaM-EGO, and BaM-rEGO nanocomposites

SEM images indicating the microstructural features of BaM-EG, BaM-EGO, and BaM-rEGO nanocomposites are shown in Fig. 6a–f, respectively. SEM micrograph of $\text{BaFe}_{12}\text{O}_{19}$ is also shown in Fig. 6g. All the micrographs of nanocomposites clearly indicated that the graphene sheets were successfully decorated with the $\text{BaFe}_{12}\text{O}_{19}$ nanoparticles consisting of small and elongated grains. It was found that the average size of $\text{BaFe}_{12}\text{O}_{19}$ nanoparticles was in the range of $70\text{--}120\text{ nm}$ [Fig. 6g], and they showed a relatively broad size distribution due to the agglomeration. It is also noteworthy that the interactions between graphene sheets and $\text{BaFe}_{12}\text{O}_{19}$ nanoparticles are sufficiently strong. As seen in Fig. 6b, agglomerated hexaferrite nanoparticles completely covered the surfaces of large graphene sheets, and the size and shape of aggregate were led by the graphene template. It should also be noted that the micropores between the graphene sheets were evenly filled up with the hexaferrite nanoparticles as clearly seen in the images of stack edges given in Fig. 6c, f. It can be concluded that the microstructural properties of graphene/ $\text{BaFe}_{12}\text{O}_{19}$ nanocomposites encourage preparing the highly porous, electromagnetically active, and structurally layered nanomaterials. It can also be concluded that such novel nanocomposites can be considered as promising material showing high microwave-absorbing performance, and the resulting “magnetic/conductive/magnetic”-layered structure of such nanocomposites could lead to multiple reflection–absorption mechanism. Figure 6h illustrates the energy dispersive spectroscopy (EDS) analysis of BaM-rEGO sample, which is a semi-quantitative microchemical analysis. It was found that the graphene amount into the composite structure was about %12. The Ba, Fe, and O

Fig. 6 SEM micrographs of **a–b** BaM-EG, **c–d** BaM-EGO, **e–f** BaM-rEGO, **g** BaFe₁₂O₁₉, and **h** EDS analysis of BaM-rEGO nanocomposite



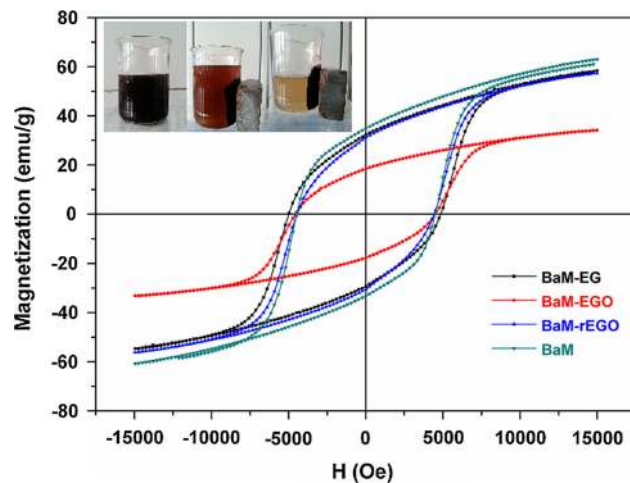


Fig. 7 Magnetic hysteresis loops of BaM-EG, BaM-EGO, and BaM-rEGO nanocomposites recorded at room temperature. The inset of photographs represents the response of BaM-rEGO suspension into water to a magnet

ratios confirmed the formation of barium hexaferrite structure.

VSM analysis

The magnetic properties of $\text{BaFe}_{12}\text{O}_{19}$ and graphene/ $\text{BaFe}_{12}\text{O}_{19}$ nanocomposites were investigated at room temperature (300 K) with an applied field being between -1.5 T and 1.5 T. Figure 6 shows the magnetic hysteresis loops of samples. As seen in Fig. 7, all samples show hard ferromagnetic property, implied with the area of the static magnetic hysteresis curve, and the high saturation magnetization (M_s) values. The M_s value can be obtained from the M versus $1/H$ curve when H goes to infinity, while coercive field (H_c) and the remanent magnetization values are directly obtained from the magnetic hysteresis curves. The M_s value of $\text{BaFe}_{12}\text{O}_{19}$ was found to be about 65 emu g^{-1} which is very close to the theoretical value of this material, 72 emu g^{-1} . The high M_s values of samples make these materials get easily separated from the aqueous dispersion by a magnet as seen in the figure inset.

It is seen in the figure that the BaM-EG and BaM-rEGO nanocomposites display very similar hysteresis and magnetic properties to the pristine $\text{BaFe}_{12}\text{O}_{19}$. The M_s , M_r , and H_c values of BaM-EG were found to be 69.4 , 32.4 emu g^{-1} , and 4920 Oe , respectively. The magnetic parameters were $M_s = 68.5$, $M_r = 31.2 \text{ emu g}^{-1}$, and $H_c \approx 4435 \text{ Oe}$ for the BaM-rEGO. On the other hand, BaM-EGO yielded the lowest M_s , M_r , and H_c values of 40.4 , 18.5 emu g^{-1} , and $H_c \approx 4548 \text{ Oe}$, respectively. The lower magnetization of BaM-EGO than other nanocomposites is possibly due to the presence of less amount of free-charge in the

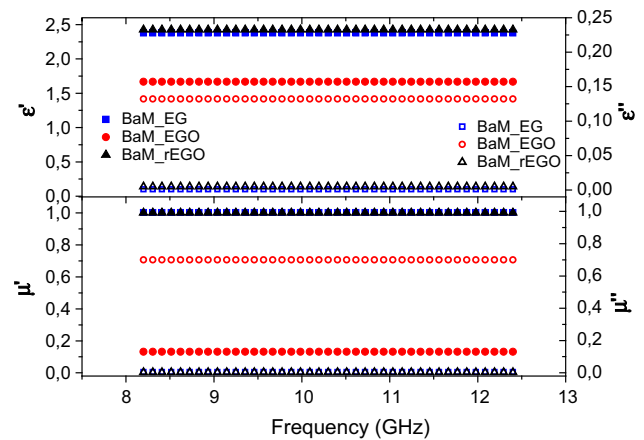


Fig. 8 The complex dielectric permittivity (ϵ' top-left axis with solid symbols and ϵ'' top-right axis with open symbols) and complex magnetic permeability (μ' bottom-left axis with solid symbols and μ'' bottom-right axis with open symbols) curves of the nanocomposites

graphene layers of such sample. Furthermore, it is obvious that the M_s depends on the mass fraction of magnetic component into the structure; thus, it can be inferred that the amount of active magnetic component, $\text{BaFe}_{12}\text{O}_{19}$, in the BaM-EGO was less than those in other nanocomposites due to the formation of BaO phase in this sample as previously mentioned based on the XRD patterns of the samples. The squareness (M_r/M_s) values of nanocomposites were determined to be about 0.46 [51].

Microwave properties of nanocomposites

The complex dielectric permittivity ($\epsilon = \epsilon' - j\epsilon''$) and magnetic permeability ($\mu = \mu' - j\mu''$) of nanocomposites were measured via Transmission Reflection Line method with the waveguide technique at X band. These parameters, shown in Fig. 8, were obtained from an Agilent 85071E Materials Measurement Software. As seen in the figure, the measured permittivity and permeability values are almost constant in the frequency range employed. The BaM-EG and BaM-rEGO nanocomposites showed approximately same dielectric permittivity of $\epsilon \approx 2.4 - j0$ and $\mu \approx 1 - j0$. One should note that the complex part of permittivity and permeability are nearly zero which is possibly due to using of small amount of powder sample in the measurements. The weight ratio of composite powder into the paraffin-based test specimen was 1:9. The technical reason for employing small amounts of sample powder in the microwave measurements is to avoid the impedance-matching problems arising from dense strong magnetic and dielectric materials. The ϵ' and μ' equations of BaM-EGO are defined as $\epsilon \approx 1.7 - j0.1$ and $\mu \approx 0.4 - j0.7$. The BaM-EGO sample yielded lower ϵ' and μ' but higher ϵ'' and μ'' values compared to the BaM-EG and BaM-rEGO

nanocomposites. This result is due to the fact that the graphene sheets were decorated with less amount of BaFe₁₂O₁₉ nanoparticle which is very consistent with the magnetization measurements. Similar relationship between the dielectric and magnetic parameters of graphene-hexagonal M-type ferrites doped with Cu and Al and the active component amount in the test specimens were reported by Bhattacharya et al. [45]. They found the complex dielectric permittivity and magnetic permeability values of such materials embedded into a thermoplastic polyurethane matrix with the graphene/hexagonal M-type ferrite ratio of 20 wt% as $\epsilon \approx 5.25-j0.15$ and $\mu \approx 1.21-j0.1$ at the frequency of 8.2 GHz. It can be concluded that the complex permittivity and permeability values are consistent

with the results as reported by Bhattacharya et al., considering that the active component (composite) ratio is 10 % in the present study. The less filling ratio reduces permittivity and permeability according to the Maxwell-Garnett effective medium theory.

The microwave-absorption properties of samples were properties were obtained from the well-known reflection loss (RL) relation given in the Eq. (2):

$$RL = 20 \log \left| \frac{Z_{in} - 1}{Z_{in} + 1} \right| \tag{2}$$

where Z_{in} is the normalized input impedance given by the following equation:

$$Z_{in} = \sqrt{\frac{\mu_r}{\epsilon_r}} \tanh \left[j \frac{2\pi d f}{c} \sqrt{\mu_r \epsilon_r} \right] \tag{3}$$

where f , d , c , ϵ_r , and μ_r are the frequency, thickness, velocity of light, complex relative permittivity, and permeability, respectively. The RL curves of nanocomposite samples are shown in Fig. 9. As seen in the figure, the RL curves of BaM-EG and BaM-rEGO showed a broad peak with the maxima of -58 dB at 11.42 GHz. On the other hand, the RL curve of BaM-EGO did not vary much within the frequency range employed. The RL peaks of BaM-EG and BaM-rEGO reduced to below -20 dB when the frequency value was of 10.14 GHz, which pointed out that the reflection was less than 1 % up to the 12.4 GHz with 2.26 GHz frequency width. The RL values below the -10 dB for the BaM-EG and BaM-rEGO signifies that such nanocomposites are promising candidates as microwave-absorbing material since they can absorb 90 % of the wave.

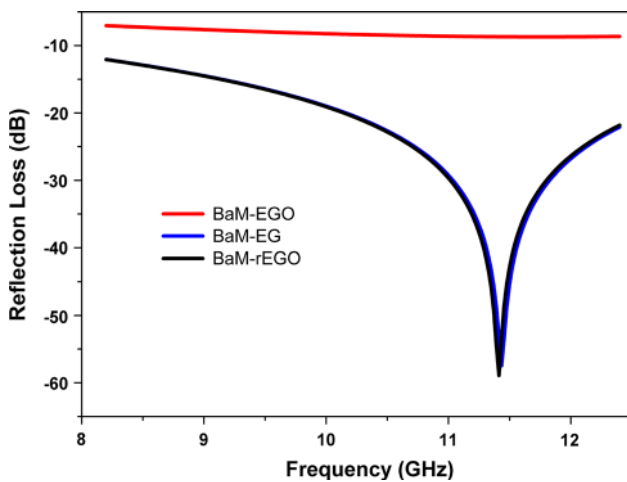
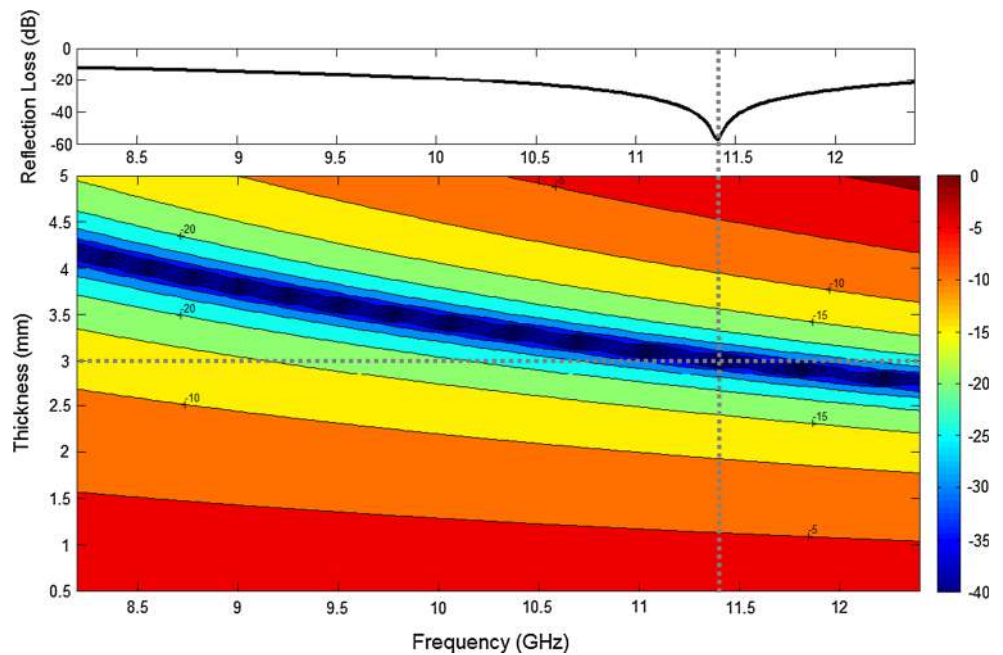


Fig. 9 The Reflection Loss curves of nanocomposites

Fig. 10 The thickness- and frequency-dependent Reflection Loss curves of BaM-rEGO nanocomposite (bottom figure) and the corresponding RL curve measured with the sample thickness of 3 mm (top figure)



In order to determine the effect of sample thickness on the microwave-absorbing performance of the sample, the RL of BaM-rEGO was calculated using the samples having the thicknesses in the range of 0.5–5.0 mm. The RL curves and the mesh plot with corresponding color bar are shown in Fig. 10. It was found that the RL decreased below the -20 dB, when the sample thickness was higher than 2.7 mm at X band and the band width was nearly same through 5 mm under -20 dB. Bhattacharya et al. also observed that the RL peak shifted to the lower frequencies with the increasing of sample thickness [45].

Conclusion

In this study, it was shown that the graphene nanosheets were successfully decorated with the hard magnetic nanoparticles, $\text{BaFe}_{12}\text{O}_{19}$, via in situ synthesis of nanoparticles by sol–gel combustion method. Magnetic characterization of nanocomposites signified that the introduction of EG and rEGO into the nanocomposite structure did not decrease the M_s value of $\text{BaFe}_{12}\text{O}_{19}$. On the other hand, EGO decreased the RL value of nanocomposite due to the presence of less amount of magnetically active material in the BaM-EGO sample compared to the other nanocomposites, which implies that the amount of hexaferrite played an important role in impedance matching. It can be concluded that the $\text{BaFe}_{12}\text{O}_{19}$ nanoparticles formed between the graphene nanosheets contribute multiple reflection to increase the absorption. Consequently, the electromagnetically active nanostructured materials having the layered structure of “magnetic/conductive/magnetic” could yield much better microwave shielding performance than the single-phase carbon materials due to the multiple reflection–absorption mechanism. The graphene/ $\text{BaFe}_{12}\text{O}_{19}$ nanocomposites are considered as promising candidate for shielding of EM waves within the microwave region based on the microstructural and physical properties of such materials.

Acknowledgements The authors thank The Research Fund of Bezmialem Vakif University (Project No. 9.2013/4) and TUBITAK, The Scientific and Technological Research Council of Turkey (Project No. 213M462) for the financial supports for the study.

References

- Pullar RC (2012) Hexagonal ferrites: a review of the synthesis, properties and applications of hexaferrite ceramics. *Prog Mater Sci* 57:1191–1334
- Sharma R, Agarwala RC, Agarwala V (2008) Development of radar absorbing nano crystals by microwave irradiation. *Mater Lett* 62:2233–2236
- Ozgur U, Alivov Y, Morkoc H (2009) Microwave ferrites, part 1: fundamental properties. *J Mater Sci-Mater Electron* 20:789–834
- Barb D, Diamandescu L, Rusi A, Tarabasanumihaila D, Morariu M, Teodorescu V (1986) Preparation of barium hexaferrite by a hydrothermal method: structure and magnetic-properties. *J Mater Sci* 21:1118–1122
- Zhong W, Ding WP, Zhang N, Hong JM, Yan QJ, Du YW (1997) Key step in synthesis of ultrafine $\text{BaFe}_{12}\text{O}_{19}$ by sol–gel technique. *J Magn Magn Mater* 168:196–202
- Tang ZX, Nafis S, Sorensen CM, Hadjipanayis GC, Klabunde KJ (1989) Magnetic properties of aerosol synthesized barium ferrite particles. *IEEE Trans Magn* 25:4236–4238
- Janasi SR, Rodrigues D, Landgraf FJG, Emura M (2000) Magnetic properties of coprecipitated barium ferrite powders as a function of synthesis conditions. *IEEE Trans Magn* 36:3327–3329
- Sozeri H (2009) Simple recipe to synthesize single-domain $\text{BaFe}_{12}\text{O}_{19}$ with high saturation magnetization. *J Magn Magn Mater* 321:2717–2722
- Pardavi-Horvath M (2000) Microwave applications of soft ferrites. *J Magn Magn Mater* 215–216:171–183
- Peddis D, Cannas C, Musinu A, Ardu A, Orru F, Fiorani D, Lauretti S, Rinaldi D, Muscas G, Concas G, Piccaluga G (2013) Beyond the effect of particle size: influence of CoFe_2O_4 nanoparticle arrangements on magnetic properties. *Chem Mater* 25:2005–2013
- Deraz NM (2010) Size and crystallinity-dependent magnetic properties of copper ferrite nano-particles. *J Alloys Compd* 501:317–325
- Chia CH, Zakaria S, Yusoff M, Goh SC, Haw CY, Ahmadi Sh, Huang NM, Lim HN (2010) Size and crystallinity-dependent magnetic properties of CoFe_2O_4 nanocrystals. *Ceram Int* 36:605–609
- Raghavender AT, Zadro K, Pajic D, Skoko Z, Biliskov N (2010) Effect of grain size on the Neel temperature of nanocrystalline nickel ferrite. *Mater Lett* 64:1144–1146
- Zhao DX, Li QL, Ye Y, Zhang CR (2010) Synthesis and characterization of carbon nanotubes decorated with strontium ferrite nanoparticles. *Synth Met* 160:866–870
- Gao C, Li WW, Morimoto H, Nagaoka Y, Maekawa T (2006) Magnetic carbon nanotubes: synthesis by electrostatic self-assembly approach and application in biomanipulations. *J Phys Chem B* 110:7213–7220
- Jia BP, Gao L, Sun J (2007) Self-assembly of magnetite beads along multiwalled carbon nanotubes via a simple hydrothermal process. *Carbon* 45:1476–1481
- Ghasemi A, Sepelak V, Liu XX, Morisako A (2011) First study on the formation of strontium ferrite thin films on functionalized multi-walled carbon nanotube. *IEEE Trans Magn* 47:2800–2803
- Ghasemi A (2011) Remarkable influence of carbon nanotubes on microwave absorption characteristics of strontium ferrite/CNT nanocomposites. *J Magn Magn Mater* 323:3133–3137
- Li QL, Ye Y, Zhao DX, Zhang W, Zhang Y (2011) Preparation and characterization of CNTs- $\text{SrFe}_{12}\text{O}_{19}$ composites. *J Alloy Compd* 509:1777–1780
- Correa-Duarte MA, Grzelczak M, Salgueirino-Maceira V, Giersig M, Liz-Marzan LM, Farle M, Sieradzki K, Diaz R (2005) Alignment of carbon nanotubes under low magnetic fields through attachment of magnetic nanoparticles. *J Phys Chem B* 109:19060–19063
- Georgakilas V, Tzitzios V, Gournis D, Petridis D (2005) Attachment of magnetic nanoparticles on carbon nanotubes and their soluble derivatives. *Chem Mater* 17:1613–1617
- He KQ, Yu LM, Sheng LM, An K, Ando Y, Zhao XL (2010) Doping effect of single-wall carbon nanotubes on the microwave absorption properties of nanocrystalline barium ferrite. *Jpn J Appl Phys* 49:125101

23. Ghasemi A, Javadpour S, Liu XX, Morisako A (2011) Magnetic and reflection loss characteristics of substituted barium ferrite/functionalized multiwalled carbon nanotube. *IEEE Trans Magn* 47:4310–4313
24. Li YQ, Huang Y, Qi SH, Niu L, Zhang YL, Wu YF (2012) Preparation, magnetic and electromagnetic properties of polyaniline/strontium ferrite/multiwalled carbon nanotubes composite. *Appl Surf Sci* 258:3659–3666
25. Geim AK, MacDonald AH (2007) Graphene: exploring carbon flatland. *Phys Today* 60:35–41
26. Geim AK, Novoselov KS (2007) The rise of graphene. *Nat Mater* 6:183–191
27. Pei SF, Cheng HM (2012) The reduction of graphene oxide. *Carbon* 50:3210–3228
28. Stankovich S, Dikin DA, Piner RD, Kohlhaas KA, Kleinhammes A, Jia Y, Wu Y, Nguyen ST, Ruoff RS (2007) Synthesis of graphene-based nanosheets via chemical reduction of exfoliated graphite oxide. *Carbon* 45:1558–1565
29. Fan ZJ, Wang K, Wei T, Yan J, Song LP, Shao B (2010) An environmentally friendly and efficient route for the reduction of graphene oxide by aluminum powder. *Carbon* 48:1686–1689
30. Soldano C, Mahmood A, Dujardin E (2010) Production, properties and potential of graphene. *Carbon* 48:2127–2150
31. He F, Lam K, Ma D, Fan JT, Chan LH, Zhang LM (2013) Fabrication of graphene nanosheet (GNS)-Fe₃O₄ hybrids and GNS-Fe₃O₄/syndiotactic polystyrene composites with high dielectric permittivity. *Carbon* 58:175–184
32. Ren LL, Huang S, Fan W, Liu TX (2011) One-step preparation of hierarchical superparamagnetic iron oxide/graphene composites via hydrothermal method. *Appl Surf Sci* 258:1132–1138
33. Li NW, Zheng MB, Chang XF, Ji GB, Lu HL, Xue LP, Pan LJ, Cao JM (2011) Preparation of magnetic CoFe₂O₄-functionalized graphene sheets via a facile hydrothermal method and their adsorption properties. *J Solid State Chem* 184:953–958
34. Fu YS, Chen HQ, Sun XQ, Wang X (2012) Combination of cobalt ferrite and graphene: high-performance and recyclable visible-light photocatalysis. *Appl Catal B* 111:280–287
35. Yao YJ, Miao SD, Liu SZ, Ma LP, Sun HQ, Wang SB (2012) Synthesis, characterization, and adsorption properties of magnetic Fe₃O₄@graphene nanocomposite. *Chem Eng J* 184:326–332
36. Xu Z, Huang YA, Yang Y, Shen JY, Tang T, Huang RS (2010) Dispersion of iron nano-particles on expanded graphite for the shielding of electromagnetic radiation. *J Magn Magn Mater* 322:3084–3087
37. Li LC, Xiang C, Qian HS, Hao B, Chen KY, Qiao R (2011) Expanded graphite/cobalt ferrite/polyaniline ternary composites: fabrication, properties, and potential applications. *J Mater Res* 26:2683–2690
38. Wang GL, Sun QR, Zhang YQ, Fan JH, Ma LM (2010) Sorption and regeneration of magnetic exfoliated graphite as a new sorbent for oil pollution. *Desalination* 263:183–188
39. Narayanan TN, Liu Z, Lakshmy PR, Gao W, Nagaoka Y, Kumar DS, Lou J, Vajtai R, Ajayan PM (2012) Synthesis of reduced graphene oxide-Fe₃O₄ multifunctional freestanding membranes and their temperature dependent electronic transport properties. *Carbon* 50:1338–1345
40. Wang QH, Wang DW, Li YQ, Wang TM (2012) Superparamagnetic magnetite nanocrystals-graphene oxide nanocomposites: facile synthesis and their enhanced electric double-layer capacitor performance. *J Nanosci Nanotechnol* 12:4583–4590
41. Xie GQ, Xi PX, Liu HY, Chen FJ, Huang L, Shi YJ, Hou FP, Zeng ZZ, Shao CW, Wang J (2012) A facile chemical method to produce superparamagnetic graphene oxide-Fe₃O₄ hybrid composite and its application in the removal of dyes from aqueous solution. *J Mater Chem* 22:1033–1039
42. Yang XY, Zhang XY, Ma YF, Huang Y, Wang YS, Chen YS (2009) Superparamagnetic graphene oxide-Fe₃O₄ nanoparticles hybrid for controlled targeted drug carriers. *J Mater Chem* 19:2710–2714
43. Bai S, Shen XP, Zhong X, Liu Y, Zhu GX, Xu X, Chen KM (2012) One-pot solvothermal preparation of magnetic reduced graphene oxide-ferrite hybrids for organic dye removal. *Carbon* 50:2337–2346
44. Yang YQ, Wang JN (2014) Synthesis and characterization of a microwave absorbing material based on magnetoplumbite ferrite and graphite nanosheet. *Mater Lett* 124:151–154
45. Bhattacharya P, Dhibar S, Hatui G, Mandal A, Das T, Das CK (2014) Graphene decorated with hexagonal shaped M-type ferrite and polyaniline wrapper: a potential candidate for electromagnetic wave absorbing and energy storage device applications. *Rsc Adv* 4:17039–17053
46. Hummers WS, Offeman RE (1958) Preparation of graphitic oxide. *J Amer Soc* 80:1339
47. Park S, An J, Potts JR, Velamakanni A, Murali S, Ruoff RS (2011) Hydrazine-reduction of graphite- and graphene oxide. *Carbon* 49:3019–3023
48. Wejrzanowski T, Pielaszek R, Opalinska A, Matysiak H, Lojkowski W, Kurzydowski KJ (2006) Quantitative methods for nanopowders characterization. *Appl Surf Sci* 253:204–208
49. Sozeri H, Durmus Z, Baykal A, Uysal E (2012) Preparation of high quality, single domain BaFe₁₂O₁₉ particles by the citrate sol-gel combustion route with an initial Fe/Ba molar ratio of 4. *Mater Sci Eng B* 177:949–955
50. Durmus Z, Kavas H, Sozeri H, Toprak MS, Aslan A, Baykal A (2012) Poly(vinyl phosphonic acid) (PVPA)-BaFe₁₂O₁₉ Nanocomposite. *J Supercond Nov Magn* 25:1185–1193
51. Sort J, Nogues J, Surinach S, Munoz JS, Baro MD, Chappel E, Dupont F, Chouteau G (2001) Coercivity and squareness enhancement in ball-milled hard magnetic-antiferromagnetic composites. *Appl Phys Lett* 79:1142–1144